PHOTONICS Research

High detectivity photodetectors based on perovskite nanowires with suppressed surface defects

GUOHUI LI,[1,†] RUI GAO,[1,†] YUE HAN,[1] AIPING ZHAI,[1] YUCHENG LIU,[2] YUE TIAN,[1] ⓘ BINING TIAN,[1] YUYING HAO,[1] SHENGZHONG LIU,[2,3,4,5] YUCHENG WU,[1,6] AND YANXIA CUI[1,*]

[1]College of Physics and Optoelectronics, Key Laboratory of Advanced Transducers and Intelligent Control System of Ministry of Education, Key Laboratory of Interface Science and Engineering in Advanced Materials of Ministry of Education, Taiyuan University of Technology, Taiyuan 030024, China
[2]Key Laboratory of Applied Surface and Colloid Chemistry, MOE; Shaanxi Key Laboratory for Advanced Energy Devices; Shaanxi Engineering Laboratory for Advanced Energy Technology, School of Materials Science and Engineering, Shaanxi Normal University, Xi'an 710119, China
[3]Dalian National Laboratory for Clean Energy; iChEM, Dalian Institute of Chemical Physics, Chinese Academy of Sciences, Dalian 116023, China
[4]University of Chinese Academy of Sciences, Beijing 100049, China
[5]e-mail: liusz@snnu.edu.cn
[6]e-mail: wyc@tyut.edu.cn
*Corresponding author: yanxiacui@gmail.com

Solution-processable, single-crystalline perovskite nanowires are ideal candidates for developing low-cost photodetectors, but their detectivities are limited due to a high level of unintentional defects. Through the surface-initiated solution-growth method, we fabricated high-quality, single-crystalline, defects-suppressed $MAPbI_3$ nanowires, which possess atomically smooth side surfaces with a surface roughness of 0.27 nm, corresponding to a carrier lifetime of 112.9 ns. By forming ohmic $MAPbI_3$/Au contacts through the dry contact method, high-performance metal–semiconductor–metal photodetectors have been demonstrated with a record large linear dynamic range of 157 dB along with a record high detectivity of 1.2×10^{14} Jones at an illumination power density of 5.5 nW/cm². Such superior photodetector performance metrics are attributed to, first, the defects-suppressed property of the as-grown $MAPbI_3$ nanowires, which leads to a quite low noise current in the dark, and second, the ohmic contact between $MAPbI_3$ and Au interfaces, which gives rise to an improved responsivity compared with the Schottky contact counterpart. The realized high-performance $MAPbI_3$ nanowire photodetector advances the development of low-cost photodetectors and has potential applications in weak-signal photodetection.   © 2020 Chinese Laser Press

https://doi.org/10.1364/PRJ.403030

1. INTRODUCTION

The emerging organic–inorganic hybrid perovskites, being regarded as one of the most promising semiconductor materials, appear to possess advantages of both inorganic and organic semiconductors [1–9]. The hybrid components enable the perovskites to exhibit excellent electronic characteristics, such as high carrier mobility, long carrier lifetime, and low trap density, just like inorganic semiconductors [10–12]. In addition, hybrid perovskite semiconductors also display such features as adjustable bandgap and low-temperature processing, similar to their organic counterparts [13–17]. Ascribed to the unique features of hybridization, perovskites have already shown bright prospects in the fields of solar cells [18–27], light-emitting diodes (LEDs) [28–31], and lasers [32–35]. Along the same lines, re-

search on perovskite photodetectors has also attracted widespread interest [2,36–40]. Various perovskites photodetectors including single-crystal, thin-film [41–46], and quantum dot [47–52] perovskite photodetectors have been successfully demonstrated. The figure of merit that characterizes a photodetector's ability to detect weak-light irradiation is the specific detectivity (D^*). Only high-quality semiconductor crystals can suppress the dark current, resulting in high-D^* photodetection performances.

Perovskite photodetectors can be categorized into different groups according to the crystalline properties of the perovskite layer. Generally, single-crystalline perovskite bulk material, wafers, and films are superior to their polycrystalline counterparts in terms of lower carrier recombination loss and longer carrier

lifetime because of a reduced density of grain boundaries and defects. Therefore, single-crystalline-based perovskite photodetectors show advantages of lower dark current, promoting the D^* as well as the linear dynamic range (LDR), which is crucial for weak-signal photodetection [53–58]. Differing from the frequently investigated bulk materials or wafers, low-dimensional perovskite nanostructures such as nanowires and nanoplatelets allow the manipulation of light at the nanoscale via naturally formed boundaries [59–62], and they also meet the need for good flexibility [63–69]. A series of different solution-processing techniques has been applied for preparing single-crystalline perovskite nanowires, based on which high-performance photodetectors have been demonstrated [63,64,67–80]. In 2016, by the blade-coating method, Jie's group achieved ordered $MAPbI_3$ wires of the micrometer scale and demonstrated photodetectors with a D^* of 5×10^{12} Jones [67]. Later, they demonstrated a type of $MAPbI_3$ nanowire photodetector with $MAPbI_3$ wires grown via the saturated-vapor-assisted solution-growth method, and obtained a D^* of 2.6×10^{13} Jones [76].

Although the state-of-the-art $MAPbI_3$ nanowire photodetectors have achieved tremendous success, most reported $MAPbI_3$ nanowires show obvious morphological imperfections, e.g., rough surface [67,69,81] and irregular facets [64,73,76], associated with unintentional surface defects. It is expected that these surface defects will certainly induce inevitable carrier recombination loss and unfavorable scattering loss, shortening the carrier lifetime as well as deteriorating the dark current. It is apparent that reducing the density of surface defects in the perovskite crystal is a promising route to lower the dark current and promote the specific D^* of perovskite photodetectors [1]. With this aim, Tang *et al.* immersed the solution-grown $MAPbI_3$ nanowires in oleic acid, bringing forward a reduced dark current as well as an increased response under illumination, so that the D^* was improved by an order of magnitude (reaching 2×10^{13} Jones), and the corresponding LDR reached 140 dB, which is the largest reported [73]. It is noticed that Song *et al.* proposed a so-called surface-initiated solution-growth strategy to produce single-crystalline $MAPbI_3$ nanowires [16,60,82], which could act as high-performance laser cavities with a quality factor as high as 3600, outperforming all the other reported $MAPbI_3$ nanocavities [83–86]. The surfaces of their nanowire products displayed an RMS roughness value as low as 4 nm, corresponding to a relatively low density of surface defects. It is expected that this type of $MAPbI_3$ nanowire with fewer surface defects may serve as a promising platform for developing photodetectors with high D^*.

In this work, based on the surface-initiated solution-growth strategy, we produced high-quality, single-crystalline $MAPbI_3$ nanowires with a carrier lifetime as long as 112.9 ns, which is around twice that of oleic acid passivated $MAPbI_3$ nanowires (51.1 ns) [73]. The atomic force microscopy (AFM) characterization indicates that the produced nanowires display atomically smooth surfaces with an RMS roughness down to 0.27 nm, an order of magnitude lower than the best result in the literature [60]. Such a smooth morphology of the as-grown $MAPbI_3$ nanowires indicates significantly minimized surface defects, accounting for the obtained long carrier lifetime. Through a dry-contact technique, we realize ohmic contacts between $MAPbI_3$ nanowires and Au electrodes, and further demonstrate high-performance photodetectors that can respond linearly to illumination with the power density varying from 5.5 nW/cm^2 to 370 mW/cm^2, corresponding to an LDR as large as 157 dB. At the lowest detectable illumination (P_{low}) of 5.5 nW/cm^2, its responsivity (R) is as high as 8.52×10^3 A/W, and its D^* derived from the measured noise current reaches 1.2×10^{14} Jones. To the best of our knowledge, our photodetector presents both the largest LDR and the highest D^* among all $MAPbI_3$ nanowire photodetector devices. Such superior photodetector performance metrics are attributed to, first, the defects-suppressed property of the as-grown $MAPbI_3$ nanowires, which leads to a quite low noise current in the dark, and second, the ohmic contact between $MAPbI_3$ and Au interfaces, which gives rise to an improved R compared with the Schottky contact counterpart. Our work contributes to the development of high-performance, next-generation, low-cost photodetectors.

2. RESULTS AND DISCUSSION

The single-crystalline $MAPbI_3$ nanowires are grown by the optimized surface-initiated solution-growth strategy as shown in Fig. 5 (Appendix A). When the coated transparent lead acetate ($PbAc_2$) solid film is immersed into the methyl ammonium iodide (MAI) solution, the $PbAc_2$ film immediately turns brown, due to the production of a thin layer of polycrystalline $MAPbI_3$ on its surface. This layer serves as a seed layer to initiate the crystal growth; hence, the strategy is referred to as the "surface-initiated solution-growth" strategy. After the reaction is finished, the product of the single-crystalline $MAPbI_3$ nanowires is harvested with an additional process of isopropanol (IPA) wash for removing the residual MAI. Our previous work concluded that the length and amount of the produced nanowires can be well controlled by the precursor concentration and the growth temperature [87]. In this work, we also investigate the influence of environmental humidity on the reaction and find that a humidity of 30% ± 2% is the optimal condition for obtaining the $MAPbI_3$ nanowire products with the highest density and best crystallinity, as shown in Fig. 6 (Appendix B). Because IPA can take up moisture from air due to its hygroscopic property, we suspect that water molecules can interact with the polycrystalline perovskite surface and localize electrons close to its surface [88], which might act as a driving force for initiating the growth of the $MAPbI_3$ nanowires. With the increase in humidity from 20% to 30%, there would be more water molecules in the IPA solution, resulting in more sites with localized electrons at the polycrystalline perovskite surface, thereby producing more $MAPbI_3$ nanowires. In comparison, at a high level of humidity (e.g., 35%), water molecules interact with each other and form a hydrogen bonded network [88]. Thus the localization of electrons at the polycrystalline perovskite surface cannot be produced efficiently, which means the favorable factor for initiating the growth of $MAPbI_3$ nanowires is weakened. As a result, the density of the $MAPbI_3$ nanowire product decreases at a high humidity of 35%.

Figure 1(a) presents a typical optical image of the as-grown $MAPbI_3$ nanowires accompanied by a few nanoplatelets on a

glass substrate. It can be seen that the prepared perovskite nanowires are rich in color because the thicknesses of the nanowires are different, and interference occurs between the beams reflected from the top and bottom surfaces of the nanowires [89]. These nanowires have flat rectangular end facets with dimensions of a few hundred nanometers as indicated by the scanning electron microscopy (SEM) images in Fig. 1(b). The transmission electron microscopy (TEM) analysis of a single $MAPbI_3$ nanowire was carried out as displayed in Fig. 1(c). A high-resolution TEM image of a single $MAPbI_3$ nanowire with the spacing of the lattice fringes measured to be ~0.31 nm is shown in Fig. 1(d), and the fringes are indexed as (004) or (220) of the tetragonal $MAPbI_3$ phase [73]. The inset of Fig. 1(d) presents the corresponding selected-area electron diffraction and fast Fourier transform (FFT) patterns. The sharp diffraction spots indicate that the synthesized $MAPbI_3$ nanowire has a tetragonal crystal structure with zone axes of [110] or [001].

The X-ray diffraction (XRD) patterns of the prepared $MAPbI_3$ nanowire are characterized as shown in Fig. 1(g), in good agreement with the corresponding simulated tetragonal-phase $MAPbI_3$ XRD pattern shown in Fig. 7 (Appendix B). Apparently, the pattern shows multiple strong diffraction peaks at [002], [110], [220], [004], etc., which can be assigned to the tetragonal phase with the space group of *I4/mcm* ($a = 8.8743$ Å and $c = 12.6708$ Å). Additionally, the split of the [220] and [004] peaks due to the ordering of MA^+ ions is clearly observed, further confirming that the as-grown $MAPbI_3$ product is of the tetragonal phase. The stronger diffraction peaks from

high-index lattice planes (e.g., [130], [224], [134], [404]) further validate the success of the growth of high-quality single-crystalline $MAPbI_3$. Here, it is noted that the IPA wash process is critical for producing a pure $MAPbI_3$ single-crystalline product (see Fig. 8 in Appendix B). To examine the composition uniformity of the as-grown $MAPbI_3$ nanowires, energy-dispersive X-ray spectroscopy (EDS) mapping was performed on the nanowire product, as shown in Fig. 9 (Appendix B). The distribution of elements indicates that Pb and I are homogeneously distributed in the individual $MAPbI_3$ nanowires and the atomic ratio of Pb to I is approximately 1:3.

An AFM analysis on a single $MAPbI_3$ nanowire on top of the PEDOT:PSS film was also carried out to further characterize the surface morphologies, as shown in Fig. 1(e). Apparently, the $MAPbI_3$ nanowire displays a steep wall, in agreement with the results of the SEM image in Fig. 1(a). Figure 1(f) indicates that the average RMS roughness of the selected nanowire region is measured to be 0.27 nm, reaching the atomically smooth level. For comparison, the AFM image of the PEDOT:PSS surface was also measured, as displayed in Fig. 10 in Appendix B (RMS: 0.16 nm), which is only a bit lower than that of the $MAPbI_3$ nanowire. Compared with the RMS value (4 nm) in a previous report [60], the present nanowire shows a much smoother surface, which should benefit from the systematic control of the reaction procedures. By fitting the transient photoluminescence (PL) spectrum of the $MAPbI_3$ nanowire [see Fig. 1(h)] with a double exponential function, which describes a fast decay resulting from bimolecular recombination and a long decay resulting from recombination of free carriers in
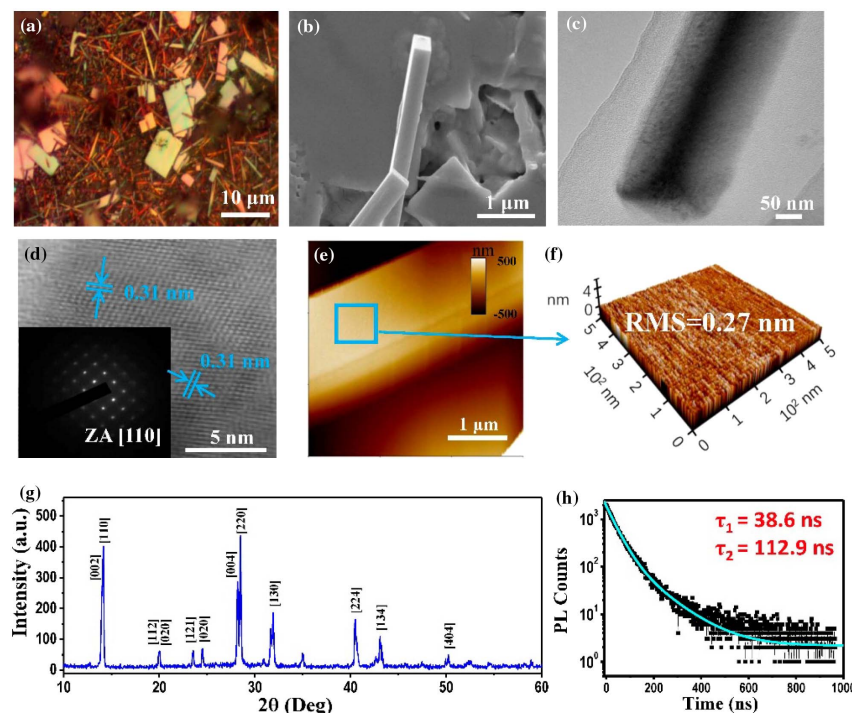

Fig. 1. (a) Optical image of $MAPbI_3$ nanostructures grown from $PbAc_2$ thin film. (b) Cross-sectional SEM image of a single $MAPbI_3$ nanowire. (c) Low-resolution TEM image of a single $MAPbI_3$ nanowire. (d) High-resolution TEM image of a selected area of a single $MAPbI_3$ nanowire; the inset represents its corresponding FFT pattern. (e) AFM image of a single $MAPbI_3$ nanowire. (f) AFM image of the selected nanowire region with the average surface roughness measured to be 0.27 nm. (g) XRD pattern of as-grown $MAPbI_3$ nanowires with a comparison of the simulated tetragonal phase $MAPbI_3$. (h) Transient PL spectrum of the $MAPbI_3$ nanowire.
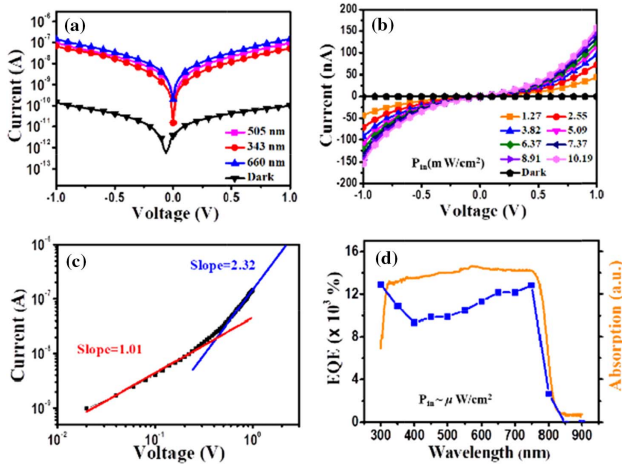
Fig. 2. (a) Logarithmic *I-V* curves under 325-nm, 505-nm, and 660-nm LED illumination at the power density of 10.19 mW/cm². (b) *I-V* curves under 660-nm illumination with different power densities. (c) Double logarithmic *I-V* plot at the power density of 10.19 mW/cm², 660 nm. (d) Wavelength-dependent EQE response and the absorption spectrum of the MAPbI$_3$ nanowire photodetector.

the radiative channel whose decay time is called the carrier lifetime, we know that the carrier lifetime of the prepared MAPbI$_3$ nanowires is 112.9 ns. Notably, the carrier lifetime of the present MAPbI$_3$ nanowires without any surface passivation is around twice that with oleic acid treatment (51 ns) [73]. Such an excellent feature of long carrier lifetime is an indicator of the significantly suppressed defects in the as-grown atomically smooth MAPbI$_3$ nanowires, enabling the products to serve as ideal candidate constituents for photodetectors with high D^*.

To construct photodetectors, high-quality, single-crystalline, defects-suppressed MAPbI$_3$ nanowires are transferred onto a glass substrate patterned with interdigitated metal electrodes through the dry-contact technique (see Appendix A for more details). To validate the photodetector performances, more than 10 photodetectors were fabricated and then analyzed for the light detection performance. The demonstrated photodetector devices are of the planar metal–semiconductor–metal (MSM) type (see Fig. 11 in Appendix C). Figure 2(a) depicts the logarithmic current–voltage (*I-V*) characteristics of the MAPbI$_3$ nanowire photodetector in the dark and under 343-nm, 505-nm, and 660-nm light illumination with a power density of 10.19 mW/cm². One sees that the photo current increases significantly with the increase in applied bias, and is much greater than the dark current. The dark current at 1 V is as low as 1×10^{-10} A; the photo current under 660-nm illumination reaches 1.47×10^{-7} A at 1 V, corresponding to a light-to-dark current ratio of 1.47×10^3. Under 660-nm illumination, as the light intensity increases, the photocurrent increases, as shown by the linear *I-V* plots in Fig. 2(b).

To analyze the contact properties, the double-logarithmic *I-V* curve at a power density of 10.19 mW/cm² under 660-nm illumination is plotted in Fig. 2(c). It is found that under higher bias, the *I-V* characteristic rises sharply, and

the fitting slopes before and after the turning voltage (V_T) are 1 and 2.3, respectively. This trend coincides with the space-charge-limited current with trap filling [90,91]. At low bias, the *I-V* current follows the ohmic response, indicating ohmic contacts are formed at the MAPbI$_3$/Au interface. After entering the space-charge-limited-current regime, the current I is approximately proportional to V^{2+n}, with n denoting the enhancement factor due to trap filling. Figure 12 (Appendix C) shows the dark and photo *I-V* characteristic of a photodetector prepared by evaporating the electrodes on top of the as-grown MAPbI$_3$ wires. It reflects that at high bias, a saturation effect of the photocurrent takes place due to the Schottky contact formed between MAPbI$_3$ nanowires and Au electrodes [57,60,87]. Differently, the suppression of photocurrent responses due to the Schottky contact can be fully eliminated in our ohmic contact MSM devices. It means that, compared with the Schottky contact, the ohmic contact between the MAPbI$_3$ and the Au enables maximization of the photocurrent responses. Moreover, it is noticed that during the process of evaporating electrodes, the MAPbI$_3$ nanowires degraded in the high temperature chamber, which also deteriorated the device stability very severely.

Next, we carried out the characterization of the LDR of the prepared MAPbI$_3$ nanowire photodetector. The LDR is defined as $20 \log(P_{sat}/P_{low})$, where P_{sat} and P_{low} represent the highest and lowest detectable illumination power densities, respectively. Outside this range, the photocurrent begins to deviate from the linear regime, and thus the light signal cannot be accurately detected. Here, we used a 532-nm laser to characterize the LDR under bias of 1 V. The power-density-dependent photocurrent curve of the demonstrated photodetector is displayed in Fig. 3(a), in which $P_{sat} = 370$ mW/cm² and $P_{low} = 5.5$ nW/cm², corresponding to an LDR of 157 dB. This LDR value exceeds that of the conventional Si-based
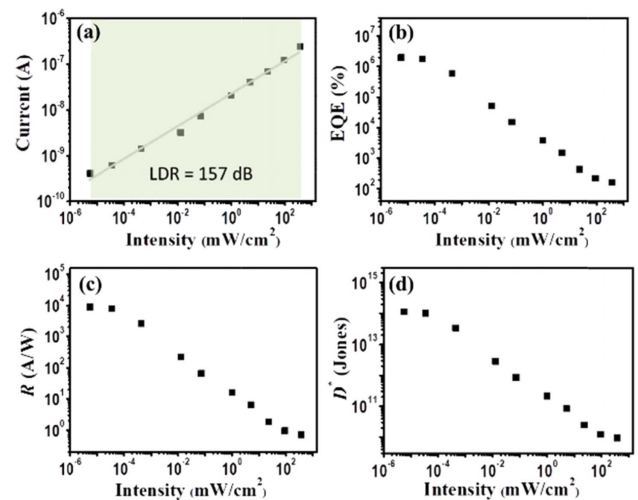

Fig. 3. (a) Current versus illumination power density (i.e., LDR measurement) of the prepared photodetector under 532-nm continuous laser illumination. (b) External quantum efficiency (EQE) versus illumination power density. (c) Responsivity (*R*) versus the illumination power density. (d) Detectivity (D^*) versus illumination power density.

Table 1. Device Performance Comparison of Different Perovskite Nanowire Photodetectors Measured at Room Temperature[a]

R (A/W)	D^* (Jones)	LDR (dB)	Response Time	Reference
1.32	2.5×10^{12}	—	T_r 0.2 ms, T_f 0.3 ms	[70]
0.1	10^{12}	—	0.3 ms	[68]
13.57	5.25×10^{12}	114	—	[67]
23	2.5×10^{11}	—	—	[71]
—	—	40	T_r 0.25 ms, T_f 0.35 ms	[69]
—	—	—	T_r 0.12 s, T_f 0.21 s	[63]
4.95	2×10^{13}	140	<0.1 ms	[73]
5.2×10^{-3}	—	—	—	[72]
—	—	—	T_r 0.12 s, T_f 0.086 s	[75]
12500	1.73×10^{11}	115	—	[64]
460	2.6×10^{13}	—	T_r 180 μs, T_f 300 μs	[76]
0.23	7.1×10^{11}	—	T_r 53.2 μs, T_f 50.2 μs	[77]
—	9.1×10^{12}	—	T_r 0.22 ms, T_f 0.79 ms	[92]
0.62	7.3×10^{12}	—	T_r 227.2 μs, T_f 215.4 μs	[79]
—	—	—	T_r 8 0 ms, T_f 140 ms	[93]
8500	1.2×10^{14}	157	T_r 350 μs, T_f 670 μs	Our results

[a]T_r and T_f represent the rise and fall times of the photodetector, respectively.

photodetector (120 dB) [2]. These demonstrated photodetectors that can detect incident light with power density varying over such a wide range are quite promising for application as power meters and imaging sensors. Our device performance is also compared with a few representative results of perovskite nanowire photodetectors from the literature, as compiled in Table 1 (Appendix C). Obviously, the LDR demonstrated in this work is up to 17 dB larger than the LDR (140 dB) of the oleic-acid-passivated MAPbI$_3$ nanowires photodetector [73]. Note that our P_{low} is two orders of magnitude lower than the previous record for all-inorganic perovskite nanowire photodetectors (10^{-4} mW/cm^2) [94] and is comparable to that of the best quasi two-dimensional perovskite nanowire photodetectors (10^{-6} mW/cm^2) [78].

From the obtained I-V measurement results, the external quantum efficiency (EQE) and R values of photodetectors under various illumination power densities are derived based on Eqs. (D1) and (D2) in Appendix D and are plotted in Figs. 2(b) and 2(c), respectively. In MSM photodetectors, it is common to see photocurrent amplification or EQE > 100% [see Eq. (D3) in Appendix D]. In this case, each photogenerated electron may induce more than one hole sweeping across the device. As observed in Fig. 3(b), at power densities from 5.5 nW/cm^2 to 370 mW/cm^2, all EQE values are greater than 100%. It is also clear that EQE and R increase with decreasing power density of the incident light, consistent with the results in the literature [95–99]. This trend is ascribed to the electron traps existing within the MAPbI$_3$ nanowires [57]. Under bias, most of the electron traps are quickly filled by the injected electrons; thus, only a small fraction of residual electron traps remain unfilled, offering opportunities for the photogenerated electrons to be trapped. With the reduction in illumination power density, due to the limited number of residual electron traps, the number of photogenerated trapped electrons per unit photon increases, and hence, EQE and R rise gradually. Consequently, at the lowest detectable power density of 5.5 nW/cm^2, one obtains the highest EQE of 2.0×10^6% and the highest R of 8.5×10^3 A/W. Here, the obtained

highest R is greater than the results of most of the MAPbI$_3$ nanowire photodetectors reported in the literature, as indicated by Table 1.

Although the previously reported MAPbI$_3$ nanowire photodetector with a record R (12.5×10^3 A/W) displayed an expected P_{low} of 10^{-4} mW/cm^2 and a measured P_{low} of 10^{-2} mW/cm^2 [64], our device exhibits a superior ability to detect weak light with four orders of magnitude lower P_{low} in comparison, due to a significantly reduced surface defect density. In our work, the as-grown single-crystalline MAPbI$_3$ nanowires have atomically smooth surfaces and regular facets, which significantly reduces the number of defects as well as the scattering loss, thereby guaranteeing the ability to distinguish very weak optical signals. In order to further confirm that our photodetectors made of atomically smooth MAPbI$_3$ nanowires are ideal candidates for detecting weak light, the noise currents are measured; hence, the device D^* can be calculated. As shown in Fig. 13 (Appendix C), the measured average noise current of the MAPbI$_3$ nanowire photodetector is ~7.2×10^{-14} A · Hz$^{-1/2}$, which is very close to the reported noise current of the oleic-acid-passivated MAPbI$_3$ nanowires [73]. This coincides with the agreement of the lowest detectable power densities of our device and the oleic-acid-passivated one. Such a low noise current should have originated from the suppressed surface defects produced by the atomically smooth surface of the MAPbI$_3$ nanowires. One sees that the noise current does not change with frequency. This reflects that the noise of this device is not dominated by the 1/f noise because the MAPbI$_3$ nanowires are of single-crystalline form, which has a near absence of grain boundaries [100–102]. For our device, the shot noise ($i_{n,s}$) and thermal noise ($i_{n,t}$) are the two main noise sources and can be derived from the dark current [see Eqs. (D4) and (D5) in Appendix D]. As shown in Fig. 2(g), the shot noise and thermal noise limits are derived to be 1.9×10^{-15} A · Hz$^{-1/2}$ and 4.3×10^{-16} A · Hz$^{-1/2}$, respectively. Taking the square root of these two noise currents, we evaluate the theoretical total noise current limit to be 1.9×10^{-15} A · Hz$^{-1/2}$, which is a bit lower than the measured noise
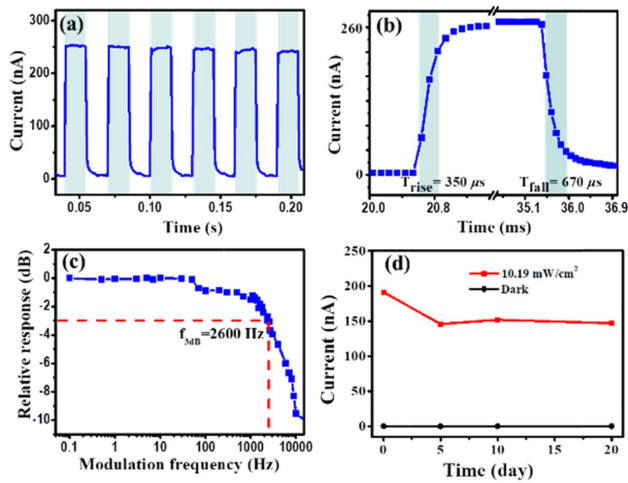
Fig. 4. (a) Transient photo response measurement of the fabricated MAPbI$_3$ nanowire photodetector under 660-nm illumination at the power density of 10.19 mW/cm^2. (b) Rise/fall time indicated in one cycle. (c) Frequency response of the MAPbI$_3$ nanowire photodetector. (d) Stability test with the photodetector stored in air at a temperature of 20°C and humidity of 10%. The prepared photodetector exhibits stable response when the illumination is turned on and off.

current of 5.7×10^{-14} A · Hz$^{-1/2}$. Thus, there is still some room for improvement in the crystalline quality and morphologies of the MAPbI$_3$ nanowires to reach the theoretical noise limit, which could be achieved by passivating the grain-boundary defect of the perovskite, interface engineering to avoid leakage currents in the detectors, etc. From the measured noise current and R, the D^* of the photodetector can be deduced [see Eq. (D7) in Appendix D]. Figure 3(d) shows that the D^* increases with decreasing power density of the incident light, and all the D^* values under illumination with the power densities from 5.5 nW/cm^2 to 370 mW/cm^2 are greater than 10^{10} Jones. At the lowest detectable illumination power density of 5.5 nW/cm^2, we obtain the highest D^* of 1.2×10^{14} Jones, outperforming all reported values of MAPbI$_3$ nanowire photodetectors, as shown in Table 1. Because the shot noise of our photodetector is one order greater than its thermal noise, the D^* can also be derived considering only the shot noise [see Eq. (D8) in Appendix D], which indicates an estimated D^* of 2.3×10^{14} Jones at the illumination power density of 5.5 nW/cm^2, comparable to that deduced from the noise current. Here, the achieved record-high D^* is attributed to the simultaneous realization of low noise current and high R, which are guaranteed by the atomically smooth surface of the as-grown MAPbI$_3$ nanowires and the long carrier lifetime, respectively, assuming ohmic contacts are formed at the MAPbI$_3$/Au interfaces.

From the I-V characterizations (see Fig. 14 in Appendix C), the wavelength-dependent EQE spectrum of the demonstrated photodetector is derived, as shown in Fig. 2(d). It can be seen that the EQE values over a broad spectral range from 300 nm to 750 nm are relatively high, in accordance with the device's broadband absorption characteristic. The rise and fall times of the MAPbI$_3$ nanowire photodetector were evaluated as

350 μs and 670 μs, respectively, corresponding to the –3-dB cutoff frequency of 2.6 kHz; see Figs. 4(a)–4(c). Here, the rise time (T_{rise}) and fall time (T_{fall}), defined as the time for the photocurrent to rise from 10% to 90% (fall from 90% to 10%) during the on and off cycles of illumination, are measured to be 350 μs and 670 μs, respectively, as shown in Fig. 4(b). The sum of the rise time and fall time, counted as the response time, equals 1020 μs, the same level as those measured values of MAPbI$_3$ nanowire photodetectors in literature [92]. Figure 4(c) shows a –3-dB cutoff frequency of 2.6 kHz, which is also comparable with the performance of other MAPbI$_3$ nanowire photodetectors [64]. Stability tests were taken every five days under 660-nm, 10.19-mW/cm^2 illumination. As displayed in Fig. 4(d), in 20 days, the dark current changed negligibly, while the photocurrent decreased to approximately 70% of its original value in the first five days and was maintained afterwards. This reveals good stability of the natural single-crystalline MAPbI$_3$ nanowire photodetectors without any passivation or capsulation processes. Moreover, the stability test results shown in Fig. 4(d) reveal that the present single-crystalline MAPbI$_3$ nanowire photodetector without any passivation or capsulation processes can maintain quite good detection ability after 20 days of storage.

3. CONCLUSION

In conclusion, high-quality single-crystalline MAPbI$_3$ nanowires with atomically smooth faces and regular facets were prepared by the surface-initiated solution-growth strategy and exhibit a carrier lifetime as long as 112.9 ns. Based on the as-grown MAPbI$_3$ nanowires, photodetectors in the MSM configuration were fabricated that exhibit excellent abilities to distinguish photo signals. The space-charge-limited-current I-V characteristic indicates that ohmic contacts are formed between the MAPbI$_3$ nanowire and Au electrodes, yielding a light-to-dark current ratio of 1470 under 660-nm illumination at a power density of 10.19 mW/cm^2. The prepared device can linearly sense light with the power density varying from 5.5×10^{-6} mW/cm^2 to 3.7×10^2 mW/cm^2, corresponding to an LDR up to 157 dB, outperforming all reported MAPbI$_3$ nanowire photodetectors. Due to the long carrier lifetime of the MAPbI$_3$ nanowires, the photo response exhibits strong amplification with the EQE exceeding 100% at all detectable power densities. When the illumination power density diminishes to 5.5×10^{-6} mW/cm^2, the photocurrent amplification effect is maximized with the external quantum efficiency and R reaching 2.0×10^6%, and 8.5×10^3 A/W, respectively. Benefiting from the significantly minimized surface defects of the MAPbI$_3$ nanowires, the measured noise current is extremely low, reaching a level of 10^{-14} A · Hz$^{-1/2}$, and, based on that, the D^* under the illumination power density of 5.5×10^{-6} mW/cm^2 is derived to be 1.2×10^{14} Jones, outperforming all reported values of MAPbI$_3$ nanowire photodetectors. Distinctly, the achieved record-high D^* results from the simultaneous realization of high R and low noise current, produced by the long carrier lifetime and suppressed defects of the as-grown MAPbI$_3$ nanowires, respectively, assuming that the MAPbI$_3$/Au contacts are of the ohmic type rather than the Schottky type. Such an outstanding performance at

weak-light detection is superior to that of all reported MAPbI$_3$ nanowire photodetectors. The proposed approach can also be applied to suppress the unintentional defects of other all-inorganic perovskite nanowires or two-dimensional perovskite nanowires, which are expected to have better stabilities than their hybrid three-dimensional perovskite counterparts. Our work contributes to the development of high-performance and low-cost photodetector devices for applications in bio-imaging sensing or long-range light communication for which weak-light signal detection is demanded.

APPENDIX A: EXPERIMENTAL METHODS

A.1. Nanowire Preparation and Device Fabrication

Single crystalline MAPbI$_3$ nanowires were synthesized using the surface initiated solution growth method, as shown in Fig. 5 [16,60,82]. First, the glass substrate was ultrasonically cleaned in deionized water, IPA, and absolute ethanol for 15 min, respectively. Then the dry substrate was treated in a plasma cleaner for 10 min to make it hydrophilic. We prepared a solution of MAI (99.5%, purchased from Xi'an Polymer Light Technology in China) in IPA at a concentration of 40 mg/mL three days in advance, and the MAI solution gradually became yellow in color before usage. In contrast, the PbAc$_2$ (99.99%, purchased from Aladdin) aqueous solution at a concentration of 140 mg/mL was used immediately after being prepared.

We placed the hydrophilic glass substrate on a hot plate at 75°C and dropped 40 μL of PbAc$_2$ solution onto it. After that, we dragged the solution of PbAc$_2$ back and forth until the deionized water was completely evaporated. Then, we put the glass substrate coated with the transparent PbAc$_2$ film into an oven at 65°C for 30 min. After the furnace was naturally cooled to room temperature, we put the substrate into the beaker containing the prepared MAI solution, and then placed the beaker in an incubator with a setting temperature. After 70 h of reaction, the growth of the single-crystalline MAPbI$_3$ nanowire product was finished. We took the glass substrate out of the beaker, and then put it in an IPA solution for 1 min to wash away the residual salt. To fabricate the photo-
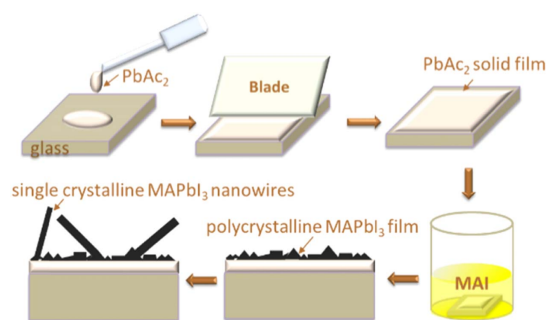

Fig. 5. Schematic illustration of the surface-initiated solution-growth strategy for preparing the single-crystalline MAPbI$_3$ nanowires. It includes mainly two steps. The first step is to coat a transparent lead acetate (PbAc$_2$) solid film based on the blade coating method, and the second step is to immerse the PbAc$_2$ film into the methyl ammonium iodide (MAI) solution at high concentration.

detectors, the as-grown MAPbI$_3$ nanowires were first transferred onto a polydimethylsiloxane (PDMS) stamp by peeling off the stamp suddenly after pressing against the glass substrate with nanowires and then transferred onto a glass substrate with a gold interdigitated electrode by peeling off slowly after using the PDMS stamp to press the substrate with the electrode. This transfer method is called the dry contact technique.

A.2. Characterization of Nanowires

The optical images of the prepared MAPbI$_3$ nanowires were characterized using an optical microscope (Nikon, LV-150). The SEM images were collected on Hitachi SU3500, and TEM images were acquired on a transmission electron microscope at an accelerating voltage of 100 kV (JEOL JEM2100). AFM images were taken by the equipment of NT-MDT Ntegra-spectra. The X-ray diffraction (XRD) patterns of the single-crystalline MAPbI$_3$ nanowires were measured by the diffractometer (Hao Yuan Instrument, DX-2700) in the θ-θ geometry to confirm the composition. The absorption spectrum of the MAPbI$_3$ nanowires was measured by an ultraviolet-visible absorption spectrometer (Shimadzu, UV-2600). The photoluminescence spectra at room temperature were recorded by a home-built fluorescence spectrophotometer system [89] using a 343 nm femtosecond laser (Light Conversion, Carbide 5W) as the excitation.

A.3. Optoelectronic Characterizations

The dark and light I-V curves and transient photo responses of MAPbI$_3$ nanowire photodetectors were characterized by placing the samples in a probe station with a shield box (PRCBE, mini) and measured using a semiconductor analyzer (Agilent, B1500). During I-V measurements, LED lamps (Thorlabs) of different wavelengths (343 nm, 505 nm, and 660 nm) were adopted as the light source with the intensities adjusted through tuning the driving voltage. The transient photo responses were acquired with LED lamps, which emit light faster than the response of the measured photodetectors. For the wavelength-dependent photo response measurement, a xenon lamp (ZOLIX GLORIA-X150A) combined with a monochromator (ZOLIX 0mni-λ 3005) was utilized. For the LDR measurement, a 532 nm continuous laser (Changchun New Industries Optoelectronics Tech. Co., Ltd.) with attenuators was used as the light source, which offered much higher power density with respect to LED lamps. The measurement of noise currents was carried out using a spectrum analyzer (Keysight 35670A) and a current amplifier (SRS SR570). The dark and light I-V curves and transient photo responses of MAPbI$_3$ nanowire photodetectors at varied temperatures were characterized by placing the samples in a cryogenic probe station (JD TMS CryoChamber-2).

APPENDIX B: GROWTH AND CHARACTERIZATION OF MAPBI$_3$ NANOWIRES UNDER DIFFERENT HUMIDITY CONDITIONS

We fixed the concentration of PbAc$_2$ solution at 100 mg/mL and studied the growth of MAPbI$_3$ nanowires under four relative humidity conditions. The four kinds of relative humidities are 20%, 25%, 30%, and 35%. Figures 6(a)–6(d) show the
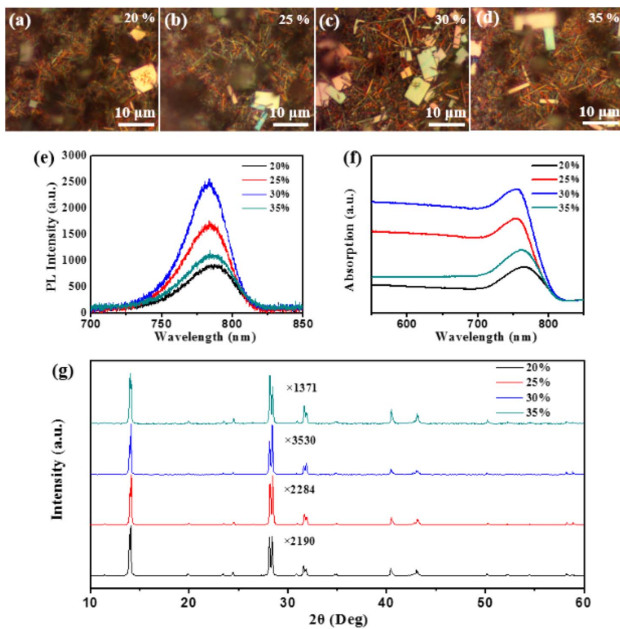
Fig. 6. (a)–(d) Optical images of MAPbI$_3$ nanowires grown from PbAc$_2$ thin film in relative humidities of 20%, 25%, 30%, and 35%. (e), (f) Corresponding absorption and PL spectra of MAPbI$_3$ nanowires grown in different humidities. (g) XRD pattern of as-grown MAPbI$_3$ nanowires with a comparison of these humidities.
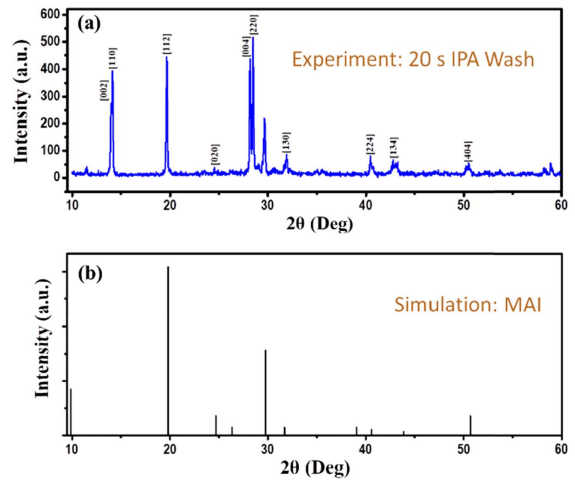

Fig. 8. (a) Experimental XRD pattern of the MAPbI$_3$ nanowires with a washing time of 20 s. (b) Simulated XRD pattern of MAI. Too short washing time (20 s) could cause a significant amount of MAI residue. The peaks at 19.8° and 29.7° in (a) indicate the existence of MAI in the final product. When the washing time is prolonged to 1 min, the pure single-crystalline MAPbI$_3$ product can be obtained.

the maximum nucleation rate, which is consistent with the results of optical images. Figure 6(g) shows the XRD pattern of the grown nanowires under these humidity conditions.
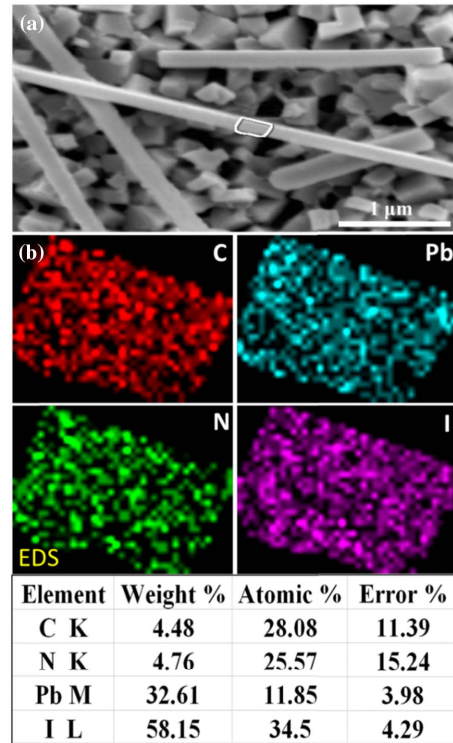
optical images of MAPbI$_3$ nanowires growing under the four relative humidities, respectively. We observe that MAPbI$_3$ nanowires have the highest density at the relative humidity of 30% in Fig. 6(c). The corresponding absorption spectrum and PL spectrum are shown in Figs. 6(e) and 6(f), respectively. It can be seen that when the relative humidity is 30% in the process of growth, the perovskite nanowires show the highest absorption intensity and PL intensity, corresponding to

Fig. 7. Experimental XRD pattern of as-grown MAPbI$_3$ nanowires with a comparison of the simulated tetragonal phase MAPbI$_3$. The as-grown MAPbI$_3$ nanowires exhibit approximately the same XRD pattern as the simulated one.

Element	Weight %	Atomic %	Error %
C K	4.48	28.08	11.39
N K	4.76	25.57	15.24
Pb M	32.61	11.85	3.98
I L	58.15	34.5	4.29

Fig. 9. Microscopic characterizations of the as-grown MAPbI$_3$ nanowires. (a) SEM image with an area of a single MAPbI$_3$ nanowire framed for the following EDS measurement. (b) EDS elemental mappings of C, Pb, N, and I, and the atomic ratios of different elements. The distribution of elements indicates that Pb and I elements are homogeneously distributed in the individual MAPbI$_3$ nanowire, and the atomic ratio between Pb and I elements is approximately 1:3.
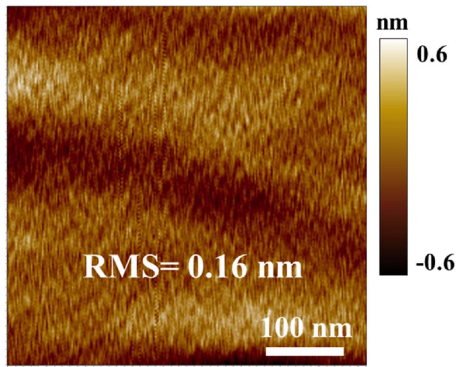
Fig. 10. AFM morphology of the PEDOT:PSS surface. It has an average RMS value of 0.16 nm, only a bit lower than that of the as-grown MAPbI₃ nanowires.

Nanowires have better crystallinity at a relative humidity of 30% with the highest diffraction peak.

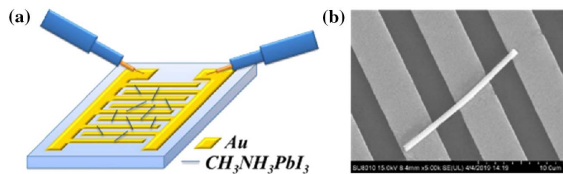## APPENDIX C: CHARACTERIZATION OF MAPBI₃ NANOWIRE PHOTODETECTORS

Fig. 11. (a) Schematic diagram of the fabricated MSM-type MAPbI₃ nanowire photodetector. (b) SEM image of a single MAPbI₃ nanowire sitting on the fingers of the interdigitated electrode. The planar metal–semiconductor–metal (MSM)-type photodetector with multiple nanowires adhered on top of the metal electrodes is fabricated. The effective photosensitive area is calculated by integrating all the areas of nanowires lying in between neighboring fingers of the electrode. At least 10 devices are fabricated for validating the calculation of the effective photosensitive area ($\sim$90 μm²).
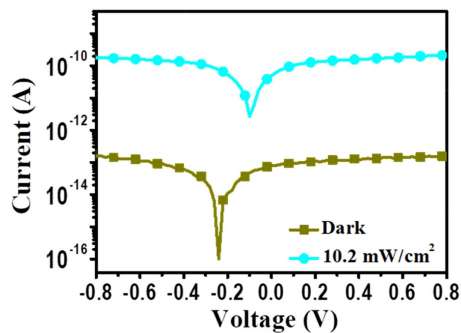

Fig. 12. Dark and photo *I-V* characteristic of a photodetector prepared by evaporating the electrodes on top of the as-grown MAPbI₃ wires.
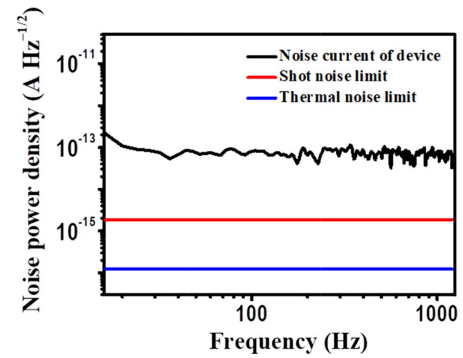

Fig. 13. Measured dark-current noise at various frequencies for the MAPbI₃ nanowire photodetector at 1 V bias. The calculated shot noise and thermal noise limits are also included for reference.
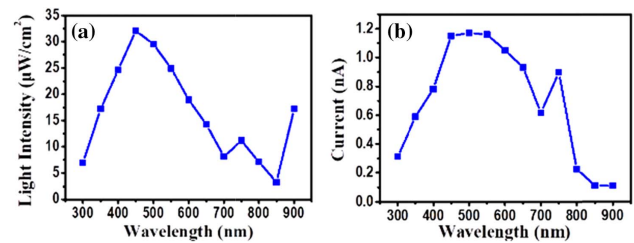

Fig. 14. (a), (b) Illumination spectrum with power densities of $\sim$μW/cm² magnitude from the Xe lamp calibrated by the power meter and the corresponding spectral photocurrent response. The wavelength-dependent photodetection capability of MAPbI₃ nanowire photodetectors is studied using the Xe lamp as the light source for *I-V* characterizations. Illumination spectrum with power densities of $\sim$μW/cm² magnitude from the Xe lamp calibrated by the power meter. It is found that our device exhibits a broadband photodetection ability from the wavelength of 300 nm to 800 nm. Here, the photocurrent at 500 nm with a power density of 29.8 μW/cm² is on the order of 1.15 nA, coincident with the LDR measurements shown in Fig. 2(d).

APPENDIX D: THEORETICAL MODEL

With *I-V* measurement results, the EQE and R of photodetectors can be derived by the following equations:

$$\text{EQE} = \frac{I_l - I_d}{P_{\text{in}} A} \frac{h\nu}{e},\tag{D1}$$

$$R = \frac{I_l - I_d}{P_{\text{in}} A},\tag{D2}$$

where I_l is the current under light illumination, I_d is the dark current, P_{in} is the illumination power density, and A is the effective photosensitive area. h is the Planck's constant, ν is the frequency of light, and e is the electron charge.

In the MSM photodetector made of MAPbI₃, the value of gain (G) is equal to EQE, which follows the formula

$$G = \text{EQE} = \frac{\mu_p \tau V_0}{L^2} = \frac{\tau}{t_p},\tag{D3}$$

where μ_p is the hole mobility, τ is the carrier lifetime, V_0 is the applied voltage, L is the electrode distance, and t_p is the transit time of the hole flowing from one electrode to another.

The shot noise ($i_{n,s}$) can be calculated from dark current using the following formula:

$$i_{n,s} = \sqrt{2ei_dB}, \qquad \text{(D4)}$$

where i_d is the dark current, e is the elementary charge, and B is the electrical bandwidth.

The thermal noise ($i_{n,t}$) is determined by the following formula:

$$i_{n,t} = \sqrt{\frac{4k_BTB}{r}}, \qquad \text{(D5)}$$

where k_B is the Boltzmann constant, T is the temperature, and r is the resistance of the MAPbI$_3$ nanowire photodetector. The total noise ($i_{n,T}$) can be calculated according to the following expression:

$$i_{n,T} = \sqrt{i_{n,s}^2 + i_{n,t}^2}. \qquad \text{(D6)}$$

Based on the measurement noise current, the D^* of the photodetector is derived by the following equation:

$$D^* = \frac{R\sqrt{AB}}{i_n}, \qquad \text{(D7)}$$

where R is the responsivity of the photodetector, B is the electrical bandwidth, and i_n is the measured dark current noise. The unit of D^* is cm · Hz$^{1/2}$/W (Jones). Considering that the noise current is generated mainly by the shot noise, the D^* can be calculated via the following formula:

$$D^* = \frac{R}{\sqrt{2eJ_d}}. \qquad \text{(D8)}$$

As indicated by Eqs. (D4) and (D5), we know that the shot noise is proportional to $i_d^{1/2}$ (i.e., inversely proportional to $r^{1/2}$), while the thermal noise is not only inversely proportional to $r^{1/2}$ but also proportional to $T^{1/2}$. As discussed in the main text, at room temperature, the shot noise is one order greater than the thermal noise. Because the proportion of the thermal noise in total noise is further inhibited with the decrease in temperature, it is reasonable to estimate the D^* at low operational temperatures considering only the shot noise.

Disclosures. The authors declare no conflicts of interest.

†These authors contributed equally to this paper.

REFERENCES

1. M. Ahmadi, T. Wu, and B. Hu, "A review on organic-inorganic halide perovskite photodetectors: device engineering and fundamental physics," Adv. Mater. **29**, 1605242 (2017).
2. L. Dou, Y. M. Yang, J. B. You, Z. R. Hong, W.-H. Chang, G. Li, and Y. Yang, "Solution-processed hybrid perovskite photodetectors with high detectivity," Nat. Commun. **5**, 5404 (2014).
3. Q. Chen, N. De Marco, Y. Yang, T.-B. Song, C. C. Chen, H. X. Zhao, Z. R. Hong, H. P. Zhou, and Y. Yang, "Under the spotlight: the organic-inorganic hybrid halide perovskite for optoelectronic applications," Nano Today **10**, 355–396 (2015).
4. Y. Zhao and K. Zhu, "Organic-inorganic hybrid lead halide perovskites for optoelectronic and electronic applications," Chem. Soc. Rev. **45**, 655–689 (2016).
5. H. Y. Xia, S. C. Tong, C. J. Zhang, C. H. Wang, J. Sun, J. He, J. Zhang, Y. L. Gao, and J. L. Yang, "Flexible and air-stable perovskite network photodetectors based on CH$_3$NH$_3$PbI$_3$/C$_8$BTBT bulk heterojunction," Appl. Phys. Lett. **112**, 233301 (2018).
6. Y. Ge, Z. Zhu, Y. Xu, Y. Chen, S. Chen, Z. Liang, Y. Song, Y. Zou, H. Zeng, S. Xu, H. Zhang, and D. Fan, "Broadband nonlinear photoresponse of 2D TiS$_2$ for ultrashort pulse generation and all-optical thresholding devices," Adv. Opt. Mater. **6**, 1701166 (2018).
7. Z. J. Xie, C. Y. Xing, W. C. Huang, T. J. Fan, Z. J. Li, J. L. Zhao, Y. J. Xiang, Z. N. Guo, J. Q. Li, Z. G. Yang, B. Q. Dong, J. L. Qu, D. Y. Fan, and H. Zhang, "Ultrathin 2D nonlayered tellurium nanosheets: facile liquid-phase exfoliation, characterization, and photoresponse with high performance and enhanced stability," Adv. Funct. Mater. **28**, 1705833 (2018).
8. B. Guo, S. H. Wang, Z. X. Wu, Z. X. Wang, D. H. Wang, H. Huang, F. Zhang, Y. Q. Ge, and H. Zhang, "Sub-200 fs soliton mode-locked fiber laser based on bismuthene saturable absorber," Opt. Express **26**, 22750–22760 (2018).
9. W. Tian, H. P. Zhou, and L. Li, "Hybrid organic-inorganic perovskite photodetectors," Small **13**, 1702107 (2017).
10. M. Chen, Y. T. Zou, L. Z. Wu, Q. Pan, D. Yang, H. C. Hu, Y. S. Tan, Q. X. Zhong, Y. Xu, H. Y. Liu, B. Q. Sun, and Q. Zhang, "Solvothermal synthesis of high-quality all-inorganic cesium lead halide perovskite nanocrystals: from nanocube to ultrathin nanowire," Adv. Funct. Mater. **27**, 1701121 (2017).
11. G. C. Xing, N. Mathews, S. Y. Sun, S. S. Lim, Y. M. Lam, M. Grätzel, S. Mhaisalkar, and T. C. Sum, "Long-range balanced electron- and hole-transport lengths in organic-inorganic CH$_3$NH$_3$PbI$_3$," Science **342**, 344–347 (2013).
12. J. Burschka, N. Pellet, S.-J. Moon, R. Humphry-Baker, P. Gao, M. K. Nazeeruddin, and M. Grätzel, "Sequential deposition as a route to high-performance perovskite-sensitized solar cells," Nature **499**, 316–319 (2013).
13. P. Wang, J. Zhang, Z. B. Zeng, R. J. Chen, X. K. Huang, L. M. Wang, J. Xu, Z. Y. Hu, and Y. J. Zhu, "Copper iodide as a potential low-cost dopant for spiro-MeOTAD in perovskite solar cells," J. Mater. Chem. C **4**, 9003–9008 (2016).
14. F. Zhang, Z. Q. Wang, H. W. Zhu, N. Pellet, J. S. Luo, C. Y. Yi, X. C. Liu, H. L. Liu, S. R. Wang, X. G. Li, Y. Xiao, S. M. Zakeeruddin, D. Q. Bi, and M. Grätzel, "Over 20% PCE perovskite solar cells with superior stability achieved by novel and low-cost hole-transporting materials," Nano Energy **41**, 469–475 (2017).
15. M. Zhang, M. Lyu, H. Yu, J. H. Yun, Q. Wang, and L. Wang, "Stable and low-cost mesoscopic CH$_3$NH$_3$PbI$_2$ Br perovskite solar cells by using a thin poly(3-hexylthiophene) layer as a hole transporter," Chemistry **21**, 434–439 (2015).
16. H. M. Zhu, Y. P. Fu, F. Meng, X. X. Wu, Z. Z. Gong, Q. Ding, M. V. Gustafsson, M. T. Trinh, S. Jin, and X.-Y. Zhu, "Lead halide perovskite nanowire lasers with low lasing thresholds and high quality factors," Nat. Mater. **14**, 636–642 (2015).
17. J. H. Noh, S. H. Im, J. H. Heo, T. N. Mandal, and S. I. Seok, "Chemical management for colorful, efficient, and stable inorganic-organic hybrid nanostructured solar cells," Nano Lett. **13**, 1764–1769 (2013).
18. J. S. Luo, J. X. Xia, H. Yang, L. L. Chen, Z. Q. Wan, F. Han, H. A. Malik, X. H. Zhu, and C. Y. Jia, "Toward high-efficiency,

hysteresis-less, stable perovskite solar cells: unusual doping of a hole-transporting material using a fluorine-containing hydrophobic Lewis acid," Energy Environ. Sci. **11**, 2035–2045 (2018).

19. R. Wang, J. J. Xue, L. Meng, J.-W. Lee, Z. P. Zhao, P. Y. Sun, L. Cai, T. Y. Huang, Z. X. Wang, Z.-K. Wang, Y. Duan, J. L. Yang, S. Tan, Y. H. Yuan, Y. Huang, and Y. Yang, "Caffeine improves the performance and thermal stability of perovskite solar cells," Joule **3**, 1464–1477 (2019).

20. Y. H. Deng, X. P. Zheng, Y. Bai, Q. Wang, J. J. Zhao, and J. S. Huang, "Surfactant-controlled ink drying enables high-speed deposition of perovskite films for efficient photovoltaic modules," Nat. Energy **3**, 560–566 (2018).

21. Y. C. Shao, Y. B. Yuan, and J. S. Huang, "Correlation of energy disorder and open-circuit voltage in hybrid perovskite solar cells," Nat. Energy **1**, 15001 (2016).

22. W. S. Yang, B.-W. Park, E. H. Jung, N. J. Jeon, Y. C. Kim, D. U. Lee, S. S. Shin, J. Seo, E. K. Kim, J. H. Noh, and S. I. Seok, "Iodide management in formamidinium-lead-halide-based perovskite layers for efficient solar cells," Science **356**, 1376–1379 (2017).

23. D. Y. Luo, W. Q. Yang, Z. P. Wang, A. Sadhanala, Q. Hu, R. Su, R. Shivanna, G. F. Trindade, J. F. Watts, Z. J. Xu, T. H. Liu, K. Chen, F. J. Ye, P. Wu, L. C. Zhao, J. Wu, Y. G. Tu, Y. F. Zhang, X. Y. Yang, W. Zhang, R. H. Friend, Q. H. Gong, H. J. Snaith, and R. Zhu, "Enhanced photovoltage for inverted planar heterojunction perovskite solar cells," Science **360**, 1442–1446 (2018).

24. C. H. Cao, C. J. Zhang, J. L. Yang, J. Sun, S. P. Pang, H. Wu, R. S. Wu, Y. L. Gao, and C. B. Liu, "Iodine and chlorine element evolution in $CH_3NH_3PbI_{3-x}Cl_x$ thin films for highly efficient planar heterojunction perovskite solar cells," Chem. Mater. **28**, 2742–2749 (2016).

25. Y. Zhao, C. J. Liang, H. M. Zhang, D. Li, D. Tian, G. B. Li, X. P. Jing, W. G. Zhang, W. K. Xiao, Q. Liu, F. J. Zhang, and Z. Q. He, "Anomalously large interface charge in polarity-switchable photovoltaic devices: an indication of mobile ions in organic-inorganic halide perovskites," Energy Environ. Sci. **8**, 1256–1260 (2015).

26. H. M. Zhang, C. J. Liang, Y. Zhao, M. J. Sun, H. Liu, J. J. Liang, D. Li, F. J. Zhang, and Z. Q. He, "Dynamic interface charge governing the current-voltage hysteresis in perovskite solar cells," Phys. Chem. Chem. Phys. **17**, 9613–9618 (2015).

27. C. W. Liu, Z. L. Qiu, W. L. Meng, J. W. Chen, J. J. Qi, C. Dong, and M. T. Wang, "Effects of interfacial characteristics on photovoltaic performance in $CH_3NH_3PbBr_3$-based bulk perovskite solar cells with core/shell nanoarray as electron transporter," Nano Energy **12**, 59–68 (2015).

28. X. L. Zhang, W. G. Wang, B. Xu, S. Liu, H. T. Dai, D. Bian, S. M. Chen, K. Wang, and X. W. Sun, "Thin film perovskite light-emitting diode based on $CsPbBr_3$ powders and interfacial engineering," Nano Energy **37**, 40–45 (2017).

29. K. B. Lin, J. Xing, L. N. Quan, F. P. G. de Arquer, X. W. Gong, J. X. Lu, L. Q. Xie, W. J. Zhao, D. Zhang, C. Z. Yan, W. Q. Li, X. Y. Liu, Y. Lu, J. Kirman, E. H. Sargent, Q. H. Xiong, and Z. H. Wei, "Perovskite light-emitting diodes with external quantum efficiency exceeding 20 per cent," Nature **562**, 245–248 (2018).

30. M. J. Yuan, L. N. Quan, R. Comin, G. Walters, R. Sabatini, O. Voznyy, S. Hoogland, Y. Zhao, E. M. Beauregard, P. Kanjanaboos, Z. H. Lu, D. H. Kim, and E. H. Sargent, "Perovskite energy funnels for efficient light-emitting diodes," Nat. Nanotechnol. **11**, 872–877 (2016).

31. A. Sultana, M. M. Alam, P. Sadhukhan, U. K. Ghorai, S. Das, T. R. Middya, and D. Mandal, "Organo-lead halide perovskite regulated green light emitting poly(vinylidene fluoride) electrospun nanofiber mat and its potential utility for ambient mechanical energy harvesting application," Nano Energy **49**, 380–392 (2018).

32. G. H. Li, T. Che, X. Q. Ji, S. D. Liu, Y. Y. Hao, Y. X. Cui, and S. Z. Liu, "Record-low-threshold lasers based on atomically smooth triangular nanoplatelet perovskite," Adv. Funct. Mater. **29**, 1805553 (2019).

33. Y. Q. Xu, Q. Chen, C. F. Zhang, R. Wang, H. Wu, X. Y. Zhang, G. C. Xing, W. W. Yu, X. Y. Wang, Y. Zhang, and M. Xiao, "Two-photon-pumped perovskite semiconductor nanocrystal lasers," J. Am. Chem. Soc. **138**, 3761–3768 (2016).

34. G. Z. Yang, H. B. Lu, F. Chen, T. Zhao, and Z. H. Chen, "Laser molecular beam epitaxy and characterization of perovskite oxide thin films," J. Cryst. Growth **227-228**, 929–935 (2001).

35. P. Li, Y. Chen, T. Yang, Z. Wang, H. Lin, Y. Xu, L. Li, H. Mu, B. N. Shivananju, Y. Zhang, Q. Zhang, A. Pan, S. Li, D. Tang, B. Jia, H. Zhang, and Q. Bao, "Two-dimensional $CH_3NH_3PbI_3$ perovskite nanosheets for ultrafast pulsed fiber lasers," ACS Appl. Mater. Interfaces **9**, 12759–12765 (2017).

36. J. Y. Liu, Y. Z. Xue, Z. Y. Wang, Z.-Q. Xu, C. X. Zheng, B. Weber, J. C. Song, Y. S. Wang, Y. R. Lu, Y. P. Zhang, and Q. L. Bao, "Two-dimensional $CH_3NH_3PbI_3$ perovskite: synthesis and optoelectronic application," ACS Nano **10**, 3536–3542 (2016).

37. C. Liu, K. Wang, P. C. Du, E. M. Wang, X. Gong, and A. J. Heeger, "Ultrasensitive solution-processed broad-band photodetectors using $CH_3NH_3PbI_3$ perovskite hybrids and PbS quantum dots as light harvesters," Nanoscale **7**, 16460–16469 (2015).

38. J. Gao, Q. B. Liang, G. H. Li, T. Ji, Y. C. Liu, M. M. Fan, Y. Y. Hao, S. Z. F. Liu, Y. C. Wu, and Y. X. Cui, "Single-crystalline lead halide perovskite wafers for high performance photodetectors," J. Mater. Chem. C **7**, 8357–8363 (2019).

39. W. Peng, L. Wang, B. Murali, K. T. Ho, A. Bera, N. Cho, C. F. Kang, V. M. Burlakov, J. Pan, L. Sinatra, C. Ma, W. Xu, D. Shi, E. Alarousu, A. Goriely, J. H. He, O. F. Mohammed, T. Wu, and O. M. Bakr, "Solution-grown monocrystalline hybrid perovskite films for hole-transporter-free solar cells," Adv. Mater. **28**, 3383–3390 (2016).

40. Y. H. Deng, Z. Q. Yang, and R. M. Ma, "Growth of centimeter-scale perovskite single-crystalline thin film via surface engineering," Nano Converg. **7**, 25 (2020).

41. Y. Liu, Q. F. Dong, Y. J. Fang, Y. Z. Lin, Y. H. Deng, and J. S. Huang, "Fast growth of thin $MAPbI_3$ crystal wafers on aqueous solution surface for efficient lateral-structure perovskite solar cells," Adv. Funct. Mater. **29**, 1807707 (2019).

42. R. Brenes, D. Guo, A. Osherov, N. K. Noel, C. Eames, E. M. Hutter, S. K. Pathak, F. Niroui, R. H. Friend, M. S. Islam, H. J. Snaith, V. Bulović, T. J. Savenije, and S. D. Stranks, "Metal halide perovskite polycrystalline films exhibiting properties of single crystals," Joule **1**, 155–167 (2017).

43. B. R. Sutherland, "Tailoring perovskite thin films to rival single crystals," Joule **1**, 23–25 (2017).

44. H. S. Rao, W. G. Li, B. X. Chen, D. B. Kuang, and C. Y. Su, "*In situ* growth of 120 cm^2 $CH_3NH_3PbBr_3$ perovskite crystal film on FTO glass for narrowband-photodetectors," Adv. Mater. **29**, 1602639 (2017).

45. Q. Lv, Z. Lian, W. He, J.-L. Sun, Q. Li, and Q. Yan, "A universal top-down approach toward thickness-controllable perovskite single-crystalline thin films," J. Mater. Chem. C **6**, 4464–4470 (2018).

46. Y. C. Liu, X. D. Ren, J. Zhang, Z. Yang, D. Yang, F. Y. Yu, J. K. Sun, C. M. Zhao, Z. Yao, B. Wang, Q. B. Wei, F. W. Xiao, H. B. Fan, H. Deng, L. P. Deng, and S. Z. F. Liu, "120 mm single-crystalline perovskite and wafers: towards viable applications," Sci. China Chem. **60**, 1367–1376 (2017).

47. J. R. Zhang, G. Hodes, Z. W. Jin, and S. Z. Liu, "All-inorganic $CsPbX_3$ perovskite solar cells: progress and prospects," Angew. Chem. Int. Ed. **58**, 15596–15618 (2019).

48. L. Zhou, K. Yu, F. Yang, J. Zheng, Y. H. Zuo, C. B. Li, B. W. Cheng, and Q. M. Wang, "All-inorganic perovskite quantum dot/mesoporous TiO_2 composite-based photodetectors with enhanced performance," Dalton Trans. **46**, 1766–1769 (2017).

49. X. Chen, D. Li, G. Pan, D. Zhou, W. Xu, J. Zhu, H. Wang, C. Chen, and H. Song, "All-inorganic perovskite quantum dot/TiO_2 inverse opal electrode platform: stable and efficient photoelectrochemical sensing of dopamine under visible irradiation," Nanoscale **10**, 10505–10513 (2018).

50. Z. Zheng, F. W. Zhuge, Y. G. Wang, J. B. Zhang, L. Gan, X. Zhou, H. Q. Li, and T. Y. Zhai, "Decorating perovskite quantum dots in TiO_2 nanotubes array for broadband response photodetector," Adv. Funct. Mater. **27**, 1703115 (2017).

51. R. Pan, H. Y. Li, J. Wang, X. Jin, Q. H. Li, Z. M. Wu, J. Gou, Y. D. Jiang, and Y. L. Song, "High-responsivity photodetectors based on

formamidinium lead halide perovskite quantum dot-graphene hybrid," Part. Part. Syst. Charact. **35**, 201700304 (2018).

52. J. Xue, Z. F. Zhu, X. B. Xu, Y. Gu, S. L. Wang, L. M. Xu, Y. S. Zou, J. Z. Song, H. B. Zeng, and Q. Chen, "Narrowband perovskite photodetector-based image array for potential application in artificial vision," Nano Lett. **18**, 7628–7634 (2018).

53. J. M. Frost, K. T. Butler, F. Brivio, C. H. Hendon, M. V. Schilfgaarde, and A. Walsh, "Atomistic origins of high-performance in hybrid halide perovskite solar cells," Nano Lett. **14**, 2584–2590 (2014).

54. S. D. Stranks, G. E. Eperon, G. Grancini, C. Menelaou, M. J. P. Alcocer, T. Leijtens, L. M. Herz, A. Petrozza, and H. J. Snaith, "Electron-hole diffusion lengths exceeding 1 micrometer in an organometal trihalide perovskite absorber," Science **342**, 341–344 (2013).

55. Q. F. Dong, Y. J. Fang, Y. C. Shao, P. Mulligan, J. Qiu, L. Cao, and J. S. Huang, "Electron-hole diffusion lengths > 175 μm in solution-grown $CH_3NH_3PbI_3$ single crystals," Science **347**, 967–970 (2015).

56. D. Shi, V. Adinolfi, R. Comin, M. Yuan, E. Alarousu, A. Buin, Y. Chen, S. Hoogland, A. Rothenberger, K. Katsiev, Y. Losovyj, X. Zhang, P. A. Dowben, O. F. Mohammed, E. H. Sargent, and O. M. Bakr, "Low trap-state density and long carrier diffusion in organolead trihalide perovskite single crystals," Science **347**, 519–522 (2015).

57. Z. P. Lian, Q. F. Yan, Q. R. Lv, Y. Wang, L. L. Liu, L. J. Zhang, S. L. Pan, Q. Li, L. D. Wang, and J. L. Sun, "High-performance planar-type photodetector on (100) facet of MAPbI_3 single crystal," Sci. Rep. **5**, 16563 (2015).

58. Y. C. Liu, Z. Yang, D. Cui, X. D. Ren, J. K. Sun, X. J. Liu, J. R. Zhang, Q. B. Wei, H. B. Fan, F. Y. Yu, X. Zhang, C. M. Zhao, and S. Z. F. Liu, "Two-inch-sized perovskite $CH_3NH_3PbX_3$ (X = Cl, Br, I) crystals: growth and characterization," Adv. Mater. **27**, 5176–5183 (2015).

59. W. M. Tian, C. Y. Zhao, J. Leng, R. R. Cui, and S. Y. Jin, "Visualizing carrier diffusion in individual single-crystal organolead halide perovskite nanowires and nanoplates," J. Am. Chem. Soc. **137**, 12458–12461 (2015).

60. R. Xiao, Y. S. Hou, Y. P. Fu, X. Y. Peng, Q. Wang, E. Gonzalez, S. Jin, and D. Yu, "Photocurrent mapping in single-crystal methylammonium lead iodide perovskite nanostructures," Nano Lett. **16**, 7710–7717 (2016).

61. S. A. Veldhuis, P. P. Boix, N. Yantara, M. Li, T. C. Sum, N. Mathews, and S. G. Mhaisalkar, "Perovskite materials for light-emitting diodes and lasers," Adv. Mater. **28**, 6804–6834 (2016).

62. M. Z. Zhong, L. Huang, H. X. Deng, X. T. Wang, B. Li, Z. M. Wei, and J. B. Li, "Flexible photodetectors based on phase dependent PbI_2 single crystals," J. Mater. Chem. C **4**, 6492–6499 (2016).

63. P. C. Zhu, S. Gu, X. P. Shen, N. Xu, Y. L. Tan, S. D. Zhuang, Y. Deng, Z. D. Lu, Z. L. Wang, and J. Zhu, "Direct conversion of perovskite thin films into nanowires with kinetic control for flexible optoelectronic devices," Nano Lett. **16**, 871–876 (2016).

64. W. Deng, L. M. Huang, X. Z. Xu, X. J. Zhang, X. C. Jin, S.-T. Lee, and J. S. Jie, "Ultrahigh-responsivity photodetectors from perovskite nanowire arrays for sequentially tunable spectral measurement," Nano Lett. **17**, 2482–2489 (2017).

65. L. Niu, Q. S. Zeng, J. Shi, C. X. Cong, C. Y. Wu, F. C. Liu, J. D. Zhou, W. Fu, Q. D. Fu, C. H. Jin, T. Yu, X. F. Liu, and Z. Liu, "Controlled growth and reliable thickness-dependent properties of organic-inorganic perovskite platelet crystal," Adv. Funct. Mater. **26**, 5263–5270 (2016).

66. J. Z. Song, L. M. Xu, J. H. Li, J. Xue, Y. H. Dong, X. M. Li, and H. B. Zeng, "Monolayer and few-layer all-inorganic perovskites as a new family of two-dimensional semiconductors for printable optoelectronic devices," Adv. Mater. **28**, 4861–4869 (2016).

67. W. Deng, X. J. Zhang, L. M. Huang, X. Z. Xu, L. Wang, J. C. Wang, Q. X. Shang, S.-T. Lee, and J. S. Jie, "Aligned single-crystalline perovskite microwire arrays for high-performance flexible image sensors with long-term stability," Adv. Mater. **28**, 2201–2208 (2016).

68. H. Deng, X. K. Yang, D. D. Dong, B. Li, D. Yang, S. J. Yuan, K. K. Qiao, Y. B. Cheng, J. Tang, and H. S. Song, "Flexible and semitransparent organolead triiodide perovskite network photodetector arrays with high stability," Nano Lett. **15**, 7963–7969 (2015).

69. E. Horváth, M. Spina, Z. Szekrényes, K. Kamarás, R. Gaal, D. Gachet, and L. S. Forro, "Nanowires of methylammonium lead iodide

70. (CH_3NH_3PbI_3) prepared by low temperature solution-mediated crystallization," Nano Lett. **14**, 6761–6766 (2014).

70. H. Deng, D. D. Dong, K. K. Qiao, L. L. Bu, B. Li, D. Yang, H. E. Wang, Y. B. Cheng, Z. X. Zhao, J. Tang, and H. S. Song, "Growth, patterning and alignment of organolead iodide perovskite nanowires for optoelectronic devices," Nanoscale **7**, 4163–4170 (2015).

71. D. D. Dong, H. Deng, C. Hu, H. B. Song, K. K. Qiao, X. K. Yang, J. Zhang, F. S. Cai, J. Tang, and H. S. Song, "Bandgap tunable $Cs_x(CH_3NH_3)_{1-x}PbI_3$ perovskite nanowires by aqueous solution synthesis for optoelectronic devices," Nanoscale **9**, 1567–1574 (2017).

72. Q. Hu, H. Wu, J. Sun, D. H. Yan, Y. L. Gao, and J. L. Yang, "Large-area perovskite nanowire arrays fabricated by large-scale roll-to-roll micro-gravure printing and doctor blading," Nanoscale **8**, 5350–5357 (2016).

73. L. Gao, K. Zeng, J. S. Guo, C. Ge, J. Du, Y. Zhao, C. Chen, H. Deng, Y. He, H. S. Song, G. D. Niu, and J. Tang, "Passivated single-crystalline $CH_3NH_3PbI_3$ nanowire photodetector with high detectivity, and polarization sensitivity," Nano Lett. **16**, 7446–7454 (2016).

74. X. Qin, Y. F. Yao, H. L. Dong, Y. G. Zhen, L. Jiang, and W. P. Hu, "Perovskite photodetectors based on $CH_3NH_3PbI_3$ single crystals," Chem. Asian J. **11**, 2675–2679 (2016).

75. S. F. Zhuo, J. F. Zhang, Y. M. Shi, Y. Huang, and B. Zhang, "Self-template-directed synthesis of porous perovskite nanowires at room temperature for high-performance visible-light photodetectors," Angew. Chem. Int. Ed. **54**, 5693–5696 (2015).

76. X. Z. Xu, X. J. Zhang, W. Deng, L. M. Huang, W. Wang, J. S. Jie, and X. H. Zhang, "Saturated vapor-assisted growth of single-crystalline organic-inorganic hybrid perovskite nanowires for high-performance photodetectors with robust stability," ACS Appl. Mater. Interfaces **10**, 10287–10295 (2018).

77. I. M. Asuo, D. Gedamua, I. Ka, L. F. Gerlein, F.-X. Fortier, A. Pignolet, S. G. Cloutier, and R. Nechachea, "High-performance pseudo-halide perovskite nanowire networks for stable and fast-response photodetector," Nano Energy **51**, 324–332 (2018).

78. J. G. Feng, C. Gong, H. F. Gao, W. Wen, Y. J. Gong, X. Y. Jiang, B. Zhang, Y. C. Wu, Y. S. Wu, H. B. Fu, L. Jiang, and X. Zhang, "Single-crystalline layered metal-halide perovskite nanowires for ultrasensitive photodetectors," Nat. Electron. **1**, 404–410 (2018).

79. I. M. Asuo, P. Fourmont, I. Ka, D. Gedamu, S. Bouzidi, A. Pignolet, R. Nechache, and S. G. Cloutier, "Highly efficient and ultrasensitive large-area flexible photodetector based on perovskite nanowires," Small **15**, 1804150 (2018).

80. H. Zhou, Z. N. Song, C. R. Grice, C. Chen, J. Zhang, Y. F. Zhu, R. H. Liu, H. Wang, and Y. F. Yan, "Self-powered $CsPbBr_3$ nanowire photodetector with a vertical structure," Nano Energy **53**, 880–886 (2018).

81. M. J. Ashley, M. N. O'Brien, K. R. Hedderick, J. A. Mason, M. B. Ross, and C. A. Mirkin, "Templated synthesis of uniform perovskite nanowire arrays," J. Am. Chem. Soc. **138**, 10096–10099 (2016).

82. Y. P. Fu, F. Meng, M. B. Rowley, B. J. Thompson, M. J. Shearer, D. Ma, R. J. Hamers, J. C. Wright, and S. Jin, "Solution growth of single crystal methylammonium lead halide perovskite nanostructures for optoelectronic and photovoltaic applications," J. Am. Chem. Soc. **137**, 5810–5818 (2015).

83. Q. Zhang, S. T. Ha, X. Liu, T. C. Sum, and Q. Xiong, "Room-temperature near-infrared high-Q perovskite whispering-gallery planar nanolasers," Nano Lett. **14**, 5995–6001 (2014).

84. Q. Liao, K. Hu, H. Zhang, X. Wang, J. Yao, and H. Fu, "Perovskite microdisk microlasers self-assembled from solution," Adv. Mater. **27**, 3405–3410 (2015).

85. J. Xing, X. F. Liu, Q. Zhang, S. T. Ha, Y. W. Yuan, C. Shen, T. C. Sum, and Q. H. Xiong, "Vapor phase synthesis of organometal halide perovskite nanowires for tunable room-temperature nanolasers," Nano Lett. **15**, 4571–4577 (2015).

86. X. Liu, L. Niu, C. Wu, C. Cong, H. Wang, Q. Zeng, H. He, Q. Fu, W. Fu, T. Yu, C. Jin, Z. Liu, and T. C. Sum, "Periodic organic-inorganic halide perovskite microplatelet arrays on silicon substrates for room-temperature lasing," Adv. Sci. **3**, 1600137 (2016).

87. R. Gao, G. H. Li, Y. Han, Y. Y. Xi, T. Ji, Y. Tian, B. N. Tian, Y. Y. Hao, Y. C. Wu, and Y. X. Cui, "Carrier lifetime exceeding 81 ns in single

crystalline perovskite nanowires enable large on-off ratio photodetectors," Org. Electron. **83**, 105744 (2020).

88. J. He, W.-H. Fang, R. Long, and O. V. Prezhdo, "Superoxide/peroxide chemistry extends charge carriers' lifetime but undermines chemical stability of $CH_3NH_3PbI_3$ exposed to oxygen: time-domain *ab initio* analysis," J. Am. Chem. Soc. **141**, 5798–5807 (2019).

89. W. M. Kong, G. H. Li, Q. B. Liang, X. Q. Ji, G. Li, T. Ji, T. Che, Y. Y. Hao, and Y. X. Cui, "Controllable deposition of regular lead iodide nanoplatelets and their photoluminescence at room temperature," Physica E **97**, 130–135 (2018).

90. J. A. Geurst, "Theory of space-charge-limited currents in thin semiconductor layers," Phys. Status Solidi B **15**, 107–118 (1966).

91. O. Marinov, M. J. Deen, and R. Datars, "Compact modeling of charge carrier mobility in organic thin-film transistors," Jpn. J. Appl. Phys. **106**, 064501 (2009).

92. Q. Zhou, J. G. Park, R. Nie, A. K. Thokchom, D. Ha, J. Pan, S. I. Seok, and T. Kim, "Nanochannel-assisted perovskite nanowires: from growth mechanisms to photodetector applications," ACS Nano **12**, 8406–8414 (2018).

93. D. Q. Zhang, L. L. Gu, Q. P. Zhang, Y. J. Lin, D.-H. Lien, M. Kam, S. Poddar, E. C. Garnett, A. Javey, and Z. Y. Fan, "Increasing photoluminescence quantum yield by nanophotonic design of quantum-confined halide perovskite nanowire arrays," Nano Lett. **19**, 2850–2857 (2019).

94. G. S. Chen, J. G. Feng, H. F. Gao, Y. J. Zhao, Y. Y. Pi, X. Y. Jiang, Y. C. Wu, and L. Jiang, "Stable alpha-$CsPbI_3$ perovskite nanowire arrays with preferential crystallographic orientation for highly sensitive photodetectors," Adv. Funct. Mater. **29**, 1808741 (2019).

95. F. W. Guo, B. Yang, Y. B. Yuan, Z. G. Xiao, Q. F. Dong, Y. Bi, and J. S. Huang, "A nanocomposite ultraviolet photodetector based on interfacial trap-controlled charge injection," Nat. Nanotechnol. **7**, 798–802 (2012).

96. O. Katz, G. Bahir, and J. Salzman, "Persistent photocurrent and surface trapping in GaN Schottky ultraviolet detectors," Appl. Phys. Lett. **84**, 4092–4094 (2004).

97. G. Konstantatos, J. Clifford, L. Levina, and E. H. Sargent, "Sensitive solution-processed visible-wavelength photodetectors," Nat. Photonics **1**, 531–534 (2007).

98. C. Soci, A. Zhang, B. Xiang, S. A. Dayeh, D. P. Aplin, J. Park, X. Y. Bao, Y. H. Lo, and D. Wang, "ZnO nanowire UV photodetectors with high internal gain," Nano Lett. **7**, 1003–1009 (2007).

99. Z. Q. Yang, Y. H. Deng, X. W. Zhang, S. Wang, H. Z. Chen, S. Yang, J. Khurgin, N. X. Fang, X. Zhang, and R. Ma, "High-performance single-crystalline perovskite thin-film photodetector," Adv. Mater. **30**, 1704333 (2018).

100. Y. C. Liu, Y. X. Zhang, Z. Yang, H. C. Ye, J. S. Feng, Z. Xu, X. Zhang, R. Munir, J. Liu, P. Zuo, Q. X. Li, M. X. Hu, L. N. Meng, K. Wang, D.-M. Smilgies, G. T. Zhao, H. Xu, Z. P. Yang, A. Amassian, J. W. Li, K. Zhao, and S. Z. F. Liu, "Multi-inch single-crystalline perovskite membrane for high-detectivity flexible photosensors," Nat. Commun. **9**, 5302 (2018).

101. W. C. Pan, H. D. Wu, J. J. Luo, Z. Z. Deng, C. Ge, C. Chen, X. W. Jiang, W. J. Yin, G. D. Niu, L. J. Zhu, L. X. Yin, Y. Zhou, Q. G. Xie, X. X. Ke, M. L. Sui, and J. Tang, "$Cs_2AgBiBr_6$ single-crystal X-ray detectors with a low detection limit," Nat. Photonics **11**, 726–732 (2017).

102. Y. J. Fang, Q. F. Dong, Y. C. Shao, Y. B. Yuan, and J. S. Huang, "Highly narrowband perovskite single-crystal photodetectors enabled by surface-charge recombination," Nat. Photonics **9**, 679–686 (2015).